REPORT DOCUMENTATION PAGE

1. REPORT DATE (DD-MM-YYYY)	2. REPORT TYPE	3. DATES COVERED (From - To)
29-11-2006	Technical paper	

4. TITLE AND SUBTITLE	5a. CONTRACT NUMBER
Numerical Prediction of UV Radiation from Two-Phase Plumes at High Altitudes (Postprint)	5b. GRANT NUMBER
	5c. PROGRAM ELEMENT NUMBER

6. AUTHOR(S)	5d. PROJECT NUMBER
Natalia E. Gimelshein, Robert B. Lyons, & James G. Reuster (ERC); Sergey F. Gimelshein (USC/Los Angeles)	5e. TASK NUMBER — 50260532
	5f. WORK UNIT NUMBER

7. PERFORMING ORGANIZATION NAME(S) AND ADDRESS(ES)	8. PERFORMING ORGANIZATION REPORT NUMBER
Air Force Research Laboratory (AFMC) AFRL/PRSA 10 E. Saturn Blvd. Edwards AFB CA 93524-7680	AFRL-PR-ED-TP-2006-455

9. SPONSORING / MONITORING AGENCY NAME(S) AND ADDRESS(ES)	10. SPONSOR/MONITOR'S ACRONYM(S)
Air Force Research Laboratory (AFMC) AFRL/PRS 5 Pollux Drive Edwards AFB CA 93524-7048	11. SPONSOR/MONITOR'S NUMBER(S) AFRL-PR-ED-TP-2006-455

12. DISTRIBUTION / AVAILABILITY STATEMENT

Approved for public release; distribution unlimited (AFRL-ERS-PAS-2006-290)

13. SUPPLEMENTARY NOTES

14. ABSTRACT

Multi-step continuum-kinetic approach is used to model a steady state plume flow from a Star 27 motor at an altitude of 118 km. Two-way coupled Navier-Stokes equations and the DSMC method are used to predict the interaction between plume and atmospheric gases and micron-sized alumina particles from the thruster. A Monte Carlo radiation code that accounts for photon scattering on particles is used to calculate UV radiation based on the obtained flowfield solutions. Comparison of computed spectral and integral radiant intensity with available flight data is performed. Photon scattering by submicron particles in the 200 nm to 400 nm range is a significant process.

15. SUBJECT TERMS

16. SECURITY CLASSIFICATION OF:			17. LIMITATION OF ABSTRACT	18. NUMBER OF PAGES	19a. NAME OF RESPONSIBLE PERSON Dr. Ingrid Wysong
a. REPORT **Unclassified**	b. ABSTRACT **Unclassified**	c. THIS PAGE **Unclassified**	SAR	15	19b. TELEPHONE NUMBER (include area code) N/A

45th AIAA Aerospace Sciences Meeting and Exhibit, 8 - 11 Jan 2007, Reno, Nevada

Numerical prediction of UV radiation from two-phase plumes at high altitudes

Natalia E. Gimelshein,[*]
Robert B. Lyons,[†]
and James G. Reuster[†]

ERC, Inc., Edwards AFB, CA 93524

Sergey F. Gimelshein[‡]

USC, Los Angeles, CA 90089

Multi-step continuum-kinetic approach is used to model a steady state plume flow from a Star 27 motor at an altitude of 118 km. Two-way coupled Navier-Stokes equations and the DSMC method are used to predict the interaction between plume and atmospheric gases and micron-sized alumina particles from the thruster. A Monte Carlo radiation code that accounts for photon scattering on particles is used to calculate UV radiation based on the obtained flowfield solutions. Comparison of computed spectral and integral radiant intensity with available flight data is performed. Photon scattering by submicron particles in the 200 nm to 400 nm range is a significant process.

I. Introduction

The success of missile signature analysis heavily depends on the reliability of signature predictions for all stages of the boost trajectory. Prediction reliability, in turn, is significantly hampered by a large number of uncertainties and unknowns currently associated with the physics and gas dynamics of rocket propulsion system exhaust plumes interacting with the surrounding atmosphere. An essential feature of solid propellant rocket plumes that complicates flow analysis is related to formation of particulates of varying types, sizes, and loadings. This makes rocket plume flows two-phase, with one phase consisting of gas atoms and molecules and the other composed of nano- and micro-scale particulates. Disregard of the two-phase character of rocket plumes usually results in unacceptable loss in prediction accuracy. The specifics of interaction between the two phases and its impact on signatures and contamination depends on the propellant composition and thruster operation. The main particulate types are soot, propellant droplet, and aluminum oxide particles.

Soot and other nano-size particles, common to liquid propellant systems, do not significantly affect the main properties of plume major gas species, and are primarily of interest due to their impact on plume radiation signatures. For low-altitude plumes, accounting for soot combustion in the mixing layer presents a considerable challenge. Remarkable progress in this field has been made since Refs. 1, 2. For high-altitude plumes, the soot combustion effects are negligible. Since the soot particles do not impact the gas flow due to their low concentration, they may be modeled in an overlay mode (although the information on gas velocity distribution functions is generally needed). Since the soot behavior is primarily dependent on the drag forces acting on it, it appears to be the least challenging problem, compared to the evolution of propellant droplets and alumina particles. There is however another aspect to soot influence on high altitude plume radiance that is much less straightforward than the drag-driven expansion; namely, heterogeneous condensation of soot particles.[3] Condensation in rocket plumes at very high altitudes (Apollo 8 translunar flight, for example) is an established fact.[4] The authors are not aware however of any detailed analysis of the relative importance of heterogeneous and conventional homogeneous condensation in plumes.

The second particulate type, unburnt drops of liquid propellants, although relatively large in size, similar to soot do not affect the bulk gas flow due to their small mass fractions; they may, however, cause significant

---

[*]Consultant

[†]Senior Aerospace Engineer, Propulsion Directorate

[‡]Research Assistant Professor, Department of Aerospace and Mechanical Engineering.

American Institute of Aeronautics and Astronautics Paper 2007-1014

contamination problems. They may also cause considerable glow radiation due to solar photon scattering on the droplets at high altitudes. The impact of the propellant droplets is expected to be much stronger in the transient flow regime, during the engine ignition and shutoff,[5] primarily due to incomplete combustion at these stages. Another potential source of liquid droplets in the plume field is from condensation, both homogeneous and heterogeneous. Since extremely low temperatures are needed for condensation to take place, this phenomenon should have a larger effect in the plumes of liquid propellant engines, due to the presence of high-temperature alumina particles in solid propellant thrusters. The impact of homogeneous condensation on high-altitude rocket plumes has been extensively studied[6,7] using the direct simulation Monte Carlo (DSMC) method. There are also a number of experimental studies where the homogeneous cluster formation was examined in various gases and conditions.[8,9] Although the exact contribution of molecular and particulate sources to surface contamination needs to be considered on a case-to-case basis, particulates generally tend to stay in the plume core flow, whereas molecular contamination may be more important for side and back flow.

Finally, aluminized solid propellant thrusters typically generate micron-sized aluminum oxide particles, with particle phase mass fractions reaching as much as 30% in the plume. The large particle phase mass fractions have a significant impact on the gas flow inside the nozzle (and therefore thruster performance), the near field plume structure, and the far field plume-atmosphere interaction structure. The strong influence from alumina particles on the flow structure inside the nozzle and in the plume results in a dramatic effect on radiation signatures, that becomes even more complex when accounting for the process of photon scattering on particles. Significant efforts have been made in the aerospace community toward accurate prediction of aluminum oxide particle impact on thruster performance and exhaust plume structure (see, for example, Ref. 10,11). The majority of the numerical efforts were focused on low-altitude flow regimes, where continuum CFD approaches are suitable throughout the flowfield. At high altitudes, the flow nonequilibrium downstream from the nozzle exit is too strong and the continuum approach becomes unsuitable for predicting plume features. A kinetic approach, such as the DSMC method, has to be used to obtain credible information on these flows. For sufficiently large thrusters, it is reasonable to use a hybrid approach that applies continuum CFD simulation to the high density nozzle flow and near field plume, and DSMC for the mid field and far field plume. The major handicap on the development of two-phase capabilities for modeling high altitude plumes is related to the lack of experimental data on particulate and gas properties, as well as multiple uncertainties in the physical models of the interaction of gaseous and particulate phases. The model deficiencies and unknown parameters result in significant numerical underprediction (four orders of magnitude for the side flow radiation[12]) as well as overprediction (up to two orders of magnitude in Ref. 13) of total and spectrally resolved radiation emission observed in flight experiments.

One of the important factors inherent in aluminized propellant plume radiation is photon scattering on alumina particles. While the contribution of this process for subscale motors (thrust level of 100 N and lower) is expected to be small (see, for example, Ref. 14), for larger motors the particulate number density is high enough for scattering to be significant. The main goal of this paper is to numerically analyze the effect of photon scattering in large rocket motors at high altitude, and compare numerical predictions of total and spectrally resolved radiation in the UV spectrum with available experimental data from the Star-27 motor firing.[15]

II.   Flow Conditions

Availability of detailed in-flight measurements of UV radiation from second and third stage plumes of the Strypi XI rocket provides a solid basis for numerical model testing and validation.[16] These measurements were conducted during the Bow Shock Ultraviolet 2 Experiment flown in early 1991. As part of this experiment, integral and spectrally resolved radiation from the Antares II motor (second stage) and the Star 27 motor (third stage) in the range from 200 to 400 nm were recorded for flight altitudes from approximately 104 km to 119 km. For data collection, aft-viewing photometers and spectrometers installed on extractable periscopes were used. Two lines of sight were examined, 4 deg and 25 deg from the rocket centerline.

In this work, the point of the flight trajectory that has been numerically examined corresponds to the Star 27 steady state operation at an altitude of 118 km. The geometric setup used to approximate experimental conditions is shown in Fig. 1a. The free stream temperature and density are 330 K and 5.21×10^{17} molecule/m^3, and the atmosphere composition is 66.7% N_2, 7.6% O_2, and 25.7% O. The rocket moves with velocity of 2850 m/s; zero angle of attack was assumed in the computations. The nozzle thrust is
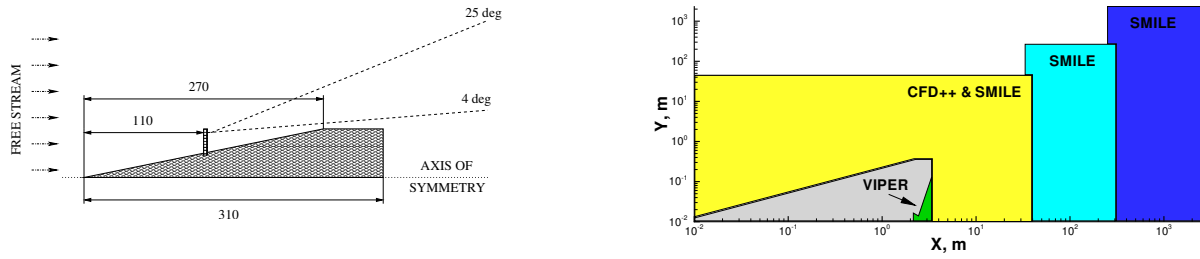
Figure 1. Schematics of the geometrical setup (left) and the computational domains used in the present multi-step approach (right).

about 5,900 lb. The exhaust gas composition is listed in Table 1. The mass fraction of the alumina particles in the exhaust is 29.5%, and the assumed particle size distribution is shown in Table 2.

Table 1. Mole fractions of major plume species.

Species	CO	CO_2	Cl	H	H_2	H_2O	HCl	OH	N_2
M.F.	0.2225	0.0291	8.67×10^{-3}	0.0190	0.2734	0.1767	0.1590	5.38×10^{-4}	0.1108

Table 2. Size distribution of alumina particles at the nozzle inlet.

Bin #	1	2	3	4	5
Diameter, μm	0.25	3.66	6.11	8.54	11.0
Mass fraction	0.10	0.40	0.30	0.15	0.05

III. Numerical Approaches

A. General numerical strategy

Modeling of a rocket plume expanding into a high altitude atmosphere is a numerically challenging problem, primarily due to the large variation in gas density and spatial scales. The flow regime varies from continuum inside the nozzle, to transitional in the near field, to free molecular in the far field of the plume. The scales of interest vary from centimeters inside the nozzle to kilometers in the plume. The change in flow regime makes application of a single numerical approach very difficult. Continuum approaches, such as those based on the solution of Navier-Stokes equations, cannot be applied to describe nonequilibrium flows in the far field of the plume. On the other hand, the use of kinetic approaches, such as direct simulation Monte Carlo (DSMC) method, to predict continuum flow inside the nozzle, although theoretically possible, is prohibitively expensive from a computational standpoint. The factor that simplifies numerical analysis is that the plume flow is typically supersonic, which means that the upstream influence of any specific point in the plume is minimal. Therefore it is both reasonable and convenient to apply a combined continuum-kinetic technique, with the continuum part of the flow being modeled by a Navier-Stokes solver, and the transitional flow computed by a kinetic method. In this work, the following combined multi-step technique, schematically illustrated in Fig. 1b, has been used.

Step 1: flow inside the nozzle. A continuum method is applied to calculate the flow inside the nozzle. The solution of the parabolized Navier-Stokes equations on a structured grid is obtained with the VIPER code for the two-phase flow inside the converging and diverging parts of the nozzle up to the nozzle exit.

Step 2: plume near field. With the macroparameters at the nozzle exit obtained at Step 1 used as the plume inflow boundary conditions, the computation of the plume near field (first 35 m downstream from the nozzle exit) is performed with a density-based Navier-Stokes solver, CFD++. Since the near field region is the most important part of the flow in terms of particle deflection by plume molecules, the computation has

also been performed using a kinetic DSMC-based solver SMILE. The DSMC computation used a starting surface at about 2 m from the nozzle exit plane, with the macroparameters at this surface obtained using CFD++.

Step 3: plume mid field. The CFD++ solution from Step 2 is used to obtain macroparameters at a new starting surface at 35 m from the nozzle exit. This surface is perpendicular to the plume axis and expands from the nozzle axis to the radial distance of 20 m. The new surface is used as the plume inflow boundary condition for a DSMC computation of the next 300 m from the nozzle exit. The velocities of molecules entering the computational domain from the starting surface were distributed according to the Maxwellian distribution. Again, the SMILE code was used in the DSMC computations.

Step 4: plume far field. The last step in the flowfield modeling is the far field computation. The DSMC method is used for this step, and the starting surface obtained from the solution of Step 3 is generated at 250 m downstream from the nozzle exit. The ellipsoidal distribution function is used for molecules entering the domain from the starting surface.

Step 5: radiation computation. The UV radiation is calculated using the flow solutions obtained at Steps 2 through 4. A Monte Carlo trajectory based code, NEMO, developed at USC is used. To compare with experimental data, spectrally resolved and integral radiation was computed along two aft-viewing lines of sight, 4° and 25° from the direction of the plume. The detector is located 1.87 m upstream from the nozzle exit plane, its radial coordinate is assumed to be 0.4 m.

Note that all starting surfaces are located in supersonic flow, with the Mach number typically much larger than unity. This guarantees a negligibly small influence of downstream regions to upstream regions, therefore providing smooth step-to-step transitions. Steps 2 through 4 modeled the interaction of the plume exhaust with the atmosphere. All steps included both gas and particulate phases.

B. Step 1: VIPER solution inside the nozzle

VIPER[4, 17] is an axisymmetric Parabolized Navier-Stokes (PNS) code that includes finite rate gas chemistry, multiphase capability (via a two-way coupled Lagrangian method), and a variety of mostly empirical models for gas-particulate interaction and particulate evolution phenomena. The PNS scheme is applied from the sonic line near the throat of the nozzle to the exit plane of the nozzle. Separate methods are provided to model the combustion chamber and converging section. The combustion chamber pressure and temperature were assumed to be 34.3 atm and 3450 K, respectively. These conditions result in an exit plane gas pressure of approximately five percent of one atmosphere, which is expected to be well within the region of applicability of this code.

C. Step 2: CFD++ modeling of plume near field

The flow solver used to perform the near-field simulation is CFD++[18, 19] developed by Metacomp Technologies, Inc. CFD++ is an unstructured, chemically reacting, multi-phase, turbulent, Reynolds Averaged Navier- Stokes (RANS) code. It uses a fully implicit, 2nd order in space, 2nd order in time, Harten, Lax, van Leer, Contact discontinuity (HLLC) Riemann approximation algorithm, and a modified two equation k-epsilon turbulence model. Finite rate chemistry is used for the simulation of the reactions. An Eulerian based Henderson drag coefficient model[20] is used for the gas-particle flow interactions. A multigrid scheme is used to speed the convergence rate. The simulation assumes that there are pre-computed nozzle inflow conditions defined at the exit plane of the nozzle. These exit plane flow conditions are obtained using the VIPER code.

All the 2D axisymmetric grids used a baseline mesh of approximately 50,000 quadrilateral nodes. For simplicity, the nozzle exit plane is assumed to be flush with the base of the vehicle. A sample of the mesh is shown in Fig. 2. Care must be taken such that the initial cell size is significantly resolved to accurately capture the dynamics of the multi-phase flow. Too large of an initial grid spacing will lead to improper particle tracking and ultimately an incorrect particle distribution. From a grid resolution study it was found that an initial grid spacing of 0.001 m was sufficient to preserve accurate particle physics.

Four unique boundary conditions are used for the axisymmetric simulations. The far field has a characteristic based inflow/outflow boundary condition imposed on it. A symmetry plane boundary condition is imposed at the center line. A Knudsen number based slip wall boundary condition is used at the body of the missile. Finally, a prescribed inflow condition is used at the exit plane of the nozzle.

American Institute of Aeronautics and Astronautics Paper 2007-1014
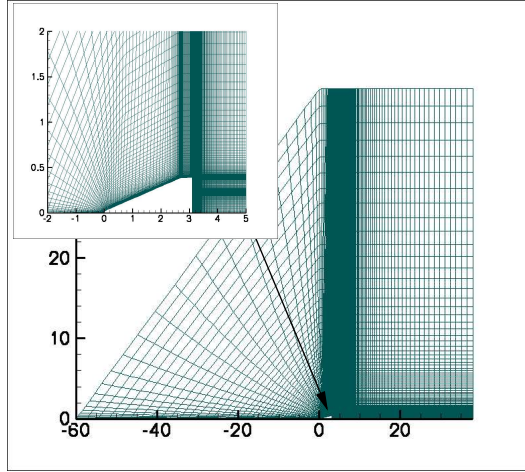
Figure 2. The mesh used in CFD++ computation of Step 2.

D.   Steps 3 and 4: SMILE simulation of the far field of the plume

The axisymmetric capability of the DSMC-based code SMILE[21] was used as the principal kinetic approach. The important features of SMILE that are relevant to this work are parallel capability, different collision and macroparameter grids with manual and automatic adaptations, and spatial weighting for axisymmetric flows. The majorant frequency scheme[22] was used to calculate intermolecular interactions. The intermolecular potential was assumed to be a variable hard sphere.[23] Energy redistribution between the internal and translational modes was performed in accordance with the Larsen-Borgnakke model. Temperature-dependent relaxation numbers were used. Species weights were used for particulate species. The particulate weights were set to 10^{-9} in Step 3 and 10^{-10} in Step 4. The reflection of molecules on the nozzle and rocket surface was assumed to be diffuse with complete energy and momentum accommodation.

The total number of simulated molecules and particulates was approximately 15 million for Step 3 and 10 million for Step 4. The number of collision cells for these cases is 4.5 and 3 million, respectively. Note that an additional calculation has been carried out for Step 3 with 5 million molecules and 1.5 million cells, and no visible difference was observed between that and the first simulation.

E.   Step 5: radiation prediction with NEMO

A parallel Monte Carlo radiation code, NEMO, has been developed at USC that has 2D and 3D modules and generally allows for prediction of radiation from two-phase rocket plumes in the UV, visible, and IR ranges. The code's line-by-line capability for the modeling of equilibrium and nonequilibrium radiation from gas media in IR has not been used in this work, and only the description of its UV capability will be given below.

Reverse Monte Carlo Method   For the calculation of radiation intensity from absorbing, emitting and scattering media, the reverse Monte Carlo method[24, 25] was used. The Reverse Monte Carlo method is based on the principle of reciprocity. The intensity at position $\mathbf{r_i}$ and direction $-\mathbf{\Omega_i}$ is calculated by emitting N rays from point $\mathbf{r_i}$ in the direction $\mathbf{\Omega_i}$ and tracing them through the medium until they reach a fully absorbing boundary. The path length between scattering events and the direction of scatter are determined from appropriate probability expressions using the local scattering coefficient σ_λ and the phase function. The intensity contributed by each individual path is found by straightening the obtained zig-zag path and performing the standard absorbing-emitting line-of-sight calculation. Since in our case boundaries of the computational domain are non-emitting, the intensity consists only of emission, attenuated by absorption, along the path:

$$I_\lambda = \int_0^l \kappa_\lambda(\mathbf{r'})I_{b\lambda}(\mathbf{r'})\exp\left[-\int_0^{l'}\kappa_\lambda(\mathbf{r''})dl''\right]dl' \tag{1}$$

where $l' = 0$ and $l'' = 0$ corresponds to point $\mathbf{r_i}$, κ_λ is local absorption coefficient and $I_{b\lambda}$ is black body intensity. The total intensity is obtained as average over N such paths.

For scattering, the Henyey-Greenstein approximation was used. The scattering and absorption coefficients and the asymmetry parameter for the particles were calculated as follows. The real part n of the complex refraction coefficient of alumina particles was calculated using the expression given in Ref. 27. The imaginary part was calculated using correlations given in Ref. 28. Then, the absorption and scattering efficiencies $Q_{abs,i}$ and $Q_{sca,i}$ as well as the asymmetry parameter g_i were calculated using the BHMIE code (originally published in Ref. 29, modified by B.T. Draine to include the calculation of asymmetry parameter g) for each particle bin. Scattering and absorption coefficients were calculated by summation over all particle bins,

$$\sigma_\lambda = \sum_{i=1}^{N_{bins}} Q_{sca,i}\pi r_i^2 n_i, \kappa_\lambda = \sum_{i=1}^{N_{bins}} Q_{abs,i}\pi r_i^2 n_i \tag{2}$$

where n_i and r_i are the number density and radius of i-th particle bin. The asymmetry factor is calculated as follows,

$$g = \frac{1}{\sigma_\lambda} \sum_{i=1}^{N_{bins}} g_i Q_{sca,i}\pi r_i^2 n_i \tag{3}$$

Since particles in different bins have different temperatures, the product $\kappa_\lambda I_{b\lambda}$ used in Eq. (1) was calculated as

$$\kappa_\lambda I_{b\lambda} = \sum_{i=1}^{N_{bins}} Q_{abs,i}\pi r_i^2 n_i I_{b\lambda}(T_i) \tag{4}$$

where $I_{b\lambda}(T_i)$ is the black body intensity calculated at a temperature of the i-th particle bin.

RADIATION CODE VALIDATION   To validate the code, reverse Monte Carlo calculations of normal radiance exiting from plane parallel media have been compared with the results obtained by Freeman et al.[26] using a reference discrete ordinate method called N-stream model. The medium optical depth is equal to 1. Because the medium is infinite along the two horizontal directions, specularly reflecting walls are used. The scattering phase function is isotropic. The radiance normalized by the black body intensity is shown in Fig. 3. It clearly shows that there is an excellent agreement between the results obtained with the different approaches.
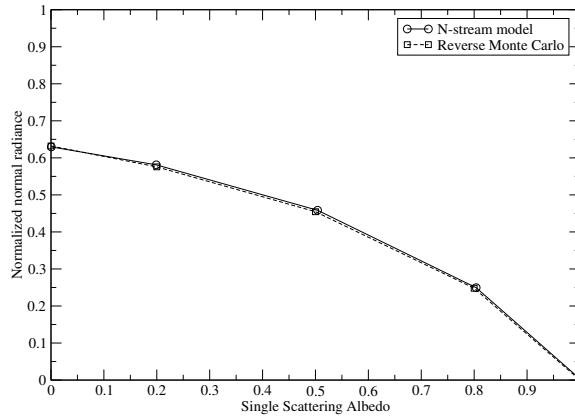
Figure 3. Normal radiance vs single scattering albedo for a uniform plane parallel medium

IV. Modeling of Plume Near Field with Kinetic and Continuum Approaches

The primary goal of this work is to estimate the effect of photon scattering from alumina particles on UV radiation in the centerline region and on the periphery of the plume. Accurate modeling of this effect requires reliable prediction of particle distribution in the plume. This is especially important for sub-micron particles as they are expected to have the most pronounced impact on scattering due to their very large number densities. The submicron particles essentially follow the gas flow inside the nozzle where the drag force dominates the particle transport. In the plume near field, and in particular in the expansion region near the nozzle lip, the gas density sharply decreases, and the inertia become more and more significant. This creates a difference between the small particle and gas flow velocities at a given position in the flow.
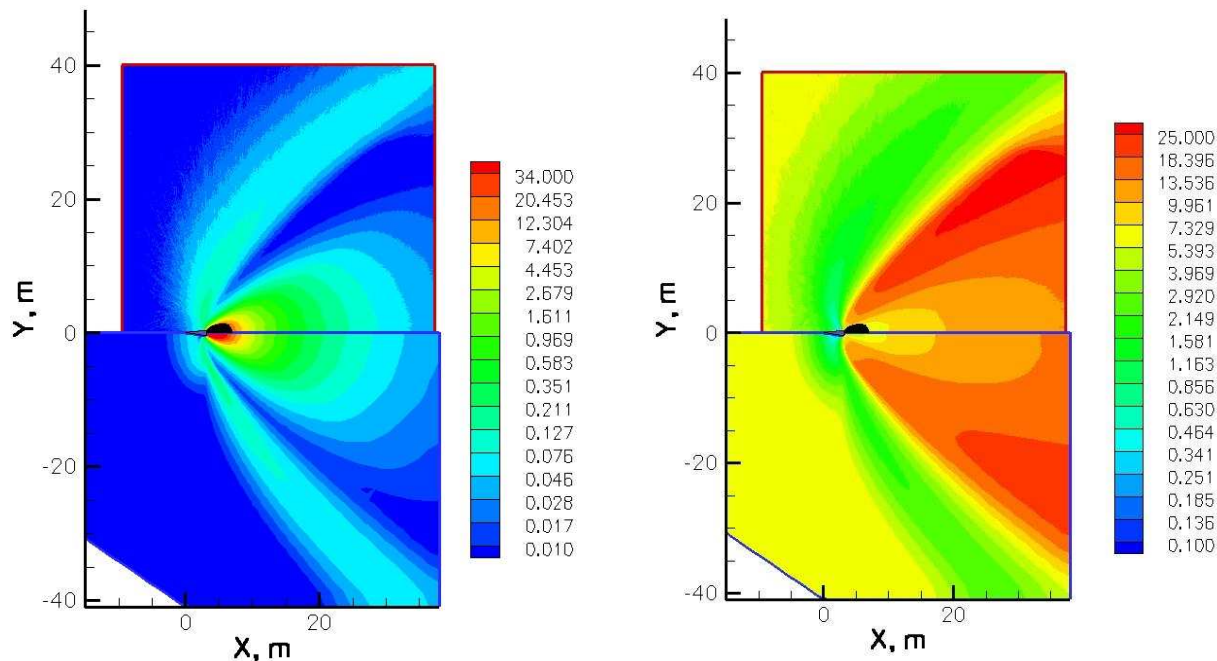

Figure 4. Near field gas pressure in Pa (left) and Mach number (right) computed with SMILE (upper parts) and CFD++ (lower parts).

To provide sufficient credibility to the plume near field solution for gas and particles, two different approaches have been utilized in this region. First, the Navier-Stokes solver CFD++ was used to compute the region of the flow starting from the nozzle exit plane and expanding 37 m downstream and 40 m in the radial direction. The region in front of the rocket was also simulated in order to include the possible impact of the free stream on the plume. Second, the DSMC solver SMILE was used in that region with the plume inflow boundary located a few meters downstream from the nozzle exit. This transfer of the DSMC inflow boundary downstream from the nozzle exit plane was necessary since the high gas density in this region makes accurate DSMC modeling in that region extremely expensive from a computational standpoint.

Comparison of gas pressure fields obtained with the kinetic and continuum approaches is presented in Fig. 4a. The rocket's leading edge is located at X=0; the black region in the DSMC part of the figure illustrates the position of the plume starting surface. There are two regions with elevated pressures, the first (inner) is due to the plume expansion, and the second (outer) corresponds to the interaction region between the hypersonic free stream and the plume. There is a reasonable agreement between the two solutions for the plume region, primarily because the flow is near equilibrium. This is not the case however for the plume-free stream interaction region. The free stream mean free path at 118 km is 3 m, which corresponds to a Knudsen number of unity based on the rocket length. This results in the formation of a viscous shock layer characterized by a bimodal molecular velocity distribution. The Navier-Stokes equations are not applicable in this case, and are known to significantly underpredict the thickness of the shock front.

This is illustrated in Fig. 4b where the Mach number field in shown. In the Navier-Stokes solution, there are two shock waves intersecting at a radial distance of approximately 10 m, the inner one from the rocket, and the outer one from the interaction of the free stream and plume molecules. In the DSMC solutions,

these shock waves merge into one, and the impact of the plume propagates as far as 10 m upstream from the rocket tip, versus about 5 m shown in the continuum solution. Similar to the pressure fields, the Mach number fields obtained with CFD++ and SMILE are close in the region of the plume, with the maximum difference not exceeding 5%.
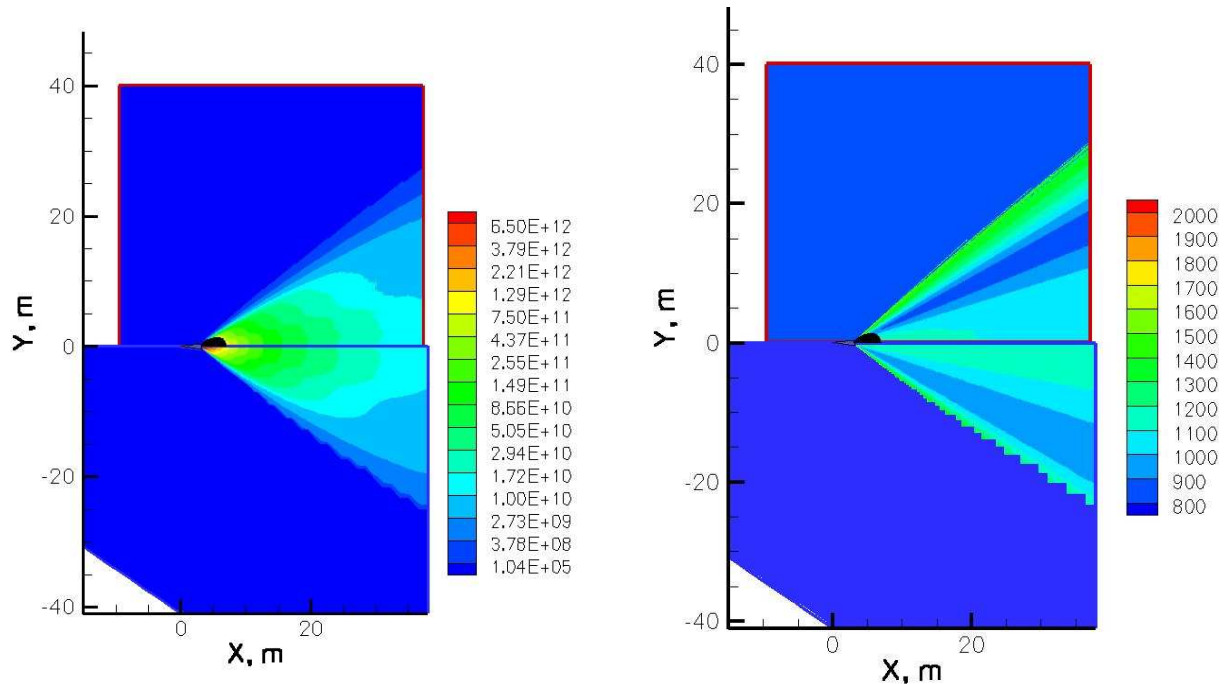
Figure 5. Near field 0.25μm particle number density per m³ (left) and surface temperature in K (right) computed with SMILE (upper parts) and CFD++ (lower parts).

The transport of submicron alumina particles near the nozzle exit plane is governed by the drag forces from the gas. The agreement between the continuum and kinetic solutions for gas properties in the plume near field region leads therefore to very good agreement in particle densities, as shown in Fig. 5a. Note that all particles stay in the plume region, and do not deflect at angles larger than 40° from the nozzle axis. Also note a significant number of particles deflected at an angle of 25°, which may lead to scattering from these particles of photons originating in the plume center back to the far field detector.

Now compare the particle temperatures fields. Comparison of DSMC and Navier-Stokes solutions is presented in Fig. 5b. Note first a strong increase of particle temperatures in the radial direction in both solutions. This increase is attributed to the weaker impact of gas cooling for particles moving at larger angles. For a given axial location in the plume, the gas density increases with the decrease in radial distance. Since the gas temperature at any particular point of the plume is lower than the corresponding particle surface temperature, particles are more effectively cooled in the center of the plume than in the periphery. The higher density gas at the plume center allows for more collisions to occur between the gas and the particles thus cooling the particles near the plume center more than those further towards the periphery. The increase of particle temperature to values over 2,000 K for the deflection angles of 45° and higher in CFD++ solution is a numerical artifact rather than a physical effect. This numerical artifact is not important, however, since there are practically no particles in this region.

Comparison of Navier-Stokes and DSMC solutions shows that the DSMC solution is characterized by up to 20% lower particle temperatures both in the core flow (4° from the nozzle axis) and in the periphery (25° from the nozzle axis). The main reason for this difference is the heat transfer model from gas to particles used in the two approaches. A similar difference has been previously observed in Ref. 14.

The gas mean free path increases from about 2 μm at the nozzle exit to hundreds of micron several meters from the nozzle exit, which means that the sub-micron particles are in the free-molecular regime relative to the particle diameter. The gas-to-particle heat transfer correlations used in CFD++ are similar to the expressions in Ref. 30 and give results close to measurements in Ref. 31. Unfortunately, in the free-molecular and near-free-molecular flow regime the applicability of this formulation is questionable and needs to be

8 of 14

American Institute of Aeronautics and Astronautics Paper 2007-1014

Distribution A: Approved for public release; distribution unlimited

further investigated. The expressions used in SMILE are accurate for the free-molecular regime, but have free parameters, namely, translational and internal energy accommodation coefficients. Due to the lack of information on gas-surface accommodation in a two-phase plume environment, the fully diffuse model was used in the present DSMC computations, although the actual reflection may have a significant degree of specularity.

Although the uncertainty in particle temperature is not critical for photon reflection by particles, it may have a significant impact on radiation predictions, especially for larger particles that are expected to be the main source of UV radiation. The temperature of these particles in the plume near field was found to be close to the melting point of 2327 K, which in part is related to the liquid-to-solid alumina phase change that occurs in that region. The number density fields for these particles are given in Fig. 6a. Due to stronger inertia of larger particles, the maximum divergence angle decreases when the particle diameter increases. For $3.66\mu m$ particles, it is still larger than the far field photometer angle of $25°$. However, the number of these particles at $25°$ is three or more orders of magnitude lower than that of the $0.25\mu m$ particles. The contribution of photon scattering and direct emission to the total radiance observed by the far field photometer will be analyzed below. The maximum deflection angle of the $6\mu m$ and larger particles is much smaller than $0.25\mu m$ particles, and they therefore do not contribute directly to the far field radiation as measured by the photometer.
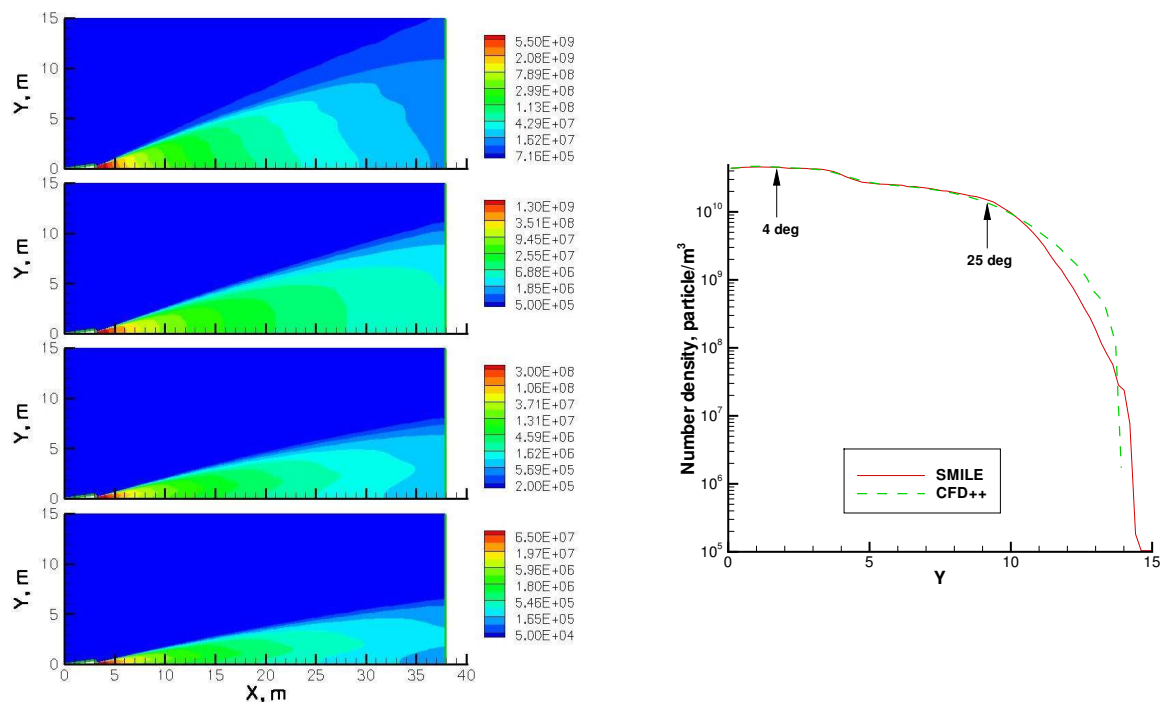
Figure 6. Left: number densities of larger particles (diameter increases from top, bin 2, to bottom, bin 5). Right: comparison of SMILE and CFD++ particle number densities (bin 1) along a radial cross section at X=20 m.

The number densities of larger particles obtained by the DSMC method are very similar to the ones given in Fig. 6a, and therefore are not shown here. Quantitative comparison of kinetic and continuum solutions is presented in Fig. 6b, where the number density profiles of $0.25\mu m$ particles are plotted along the radial direction at 16.9 m downstream from the nozzle exit plane. The location Y=0 corresponds to the plume axis. For most of the flow, especially near the nozzle axis, the solutions agree well within a few percent. There is a noticeable difference for divergence angles larger than $30°$, where the particle number density is relatively small. Although differences in the drag models and poor statistics for larger angles in DSMC are believed to be the main reasons for this difference, additional efforts need to be taken to better understand it.

American Institute of Aeronautics and Astronautics Paper 2007-1014

Distribution A: Approved for public release; distribution unlimited

V. Modeling of Plume Far Field

The near field computations presented in the previous section were used to generate starting surfaces for successive mid-field, and then far field computations. The DSMC method was used in the latter computations. The computational domains used in near and far field computations are shown in Fig. 7a, where the gas total number densities are plotted. Note that the computational domains overlap. These overlap regions were used to check whether an upstream solution agrees with a downstream one. The good agreement observed between the solutions in the overlap domains serves as the verification of the multi-step approach. The higher and lower dashed lines in this figure illustrate 4° and 25° lines of sight corresponding to the near field and far field photometers.
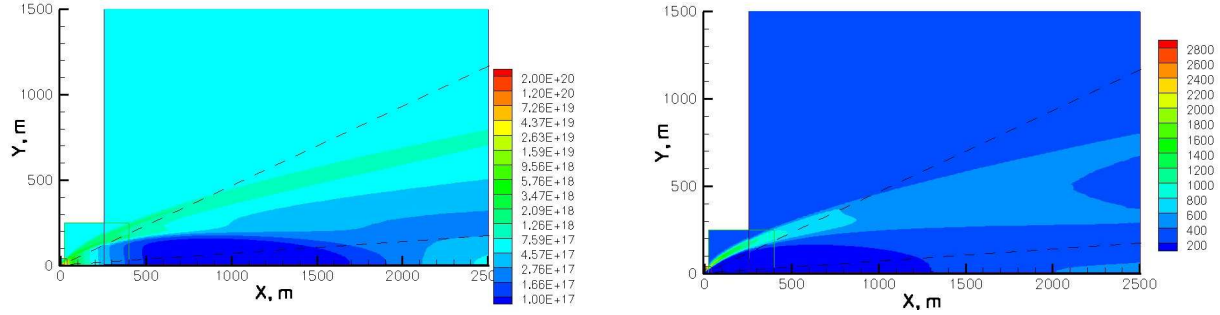

Figure 7. Gas number density in molecule/m^3 (left) and translational temperature in K (right).

Initially the highly underexpanded plume becomes overexpanded at distances larger than two hundred meters from the nozzle exit. This overexpansion results in the formation of a weak compression region near the nozzle axis approximately two kilometers downstream from the nozzle. The compression region produced due to the free stream-plume interaction, that confines the gas part of the plume, is also clearly visible. The plume-free stream compression region is characterized by elevated gas temperatures, as clearly shown in Fig. 7b. The maximum translational temperatures reach over 1000 K in this region. These temperatures are still not high enough to result in enough collisions to produce a significant increase in vibrational temperature. The vibrational temperature is near to its free molecular values for free stream molecules, and plume exhaust values for plume species.
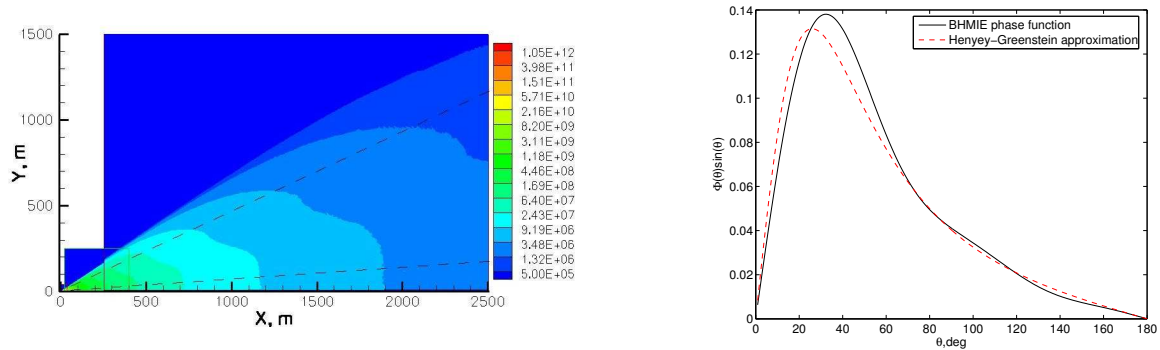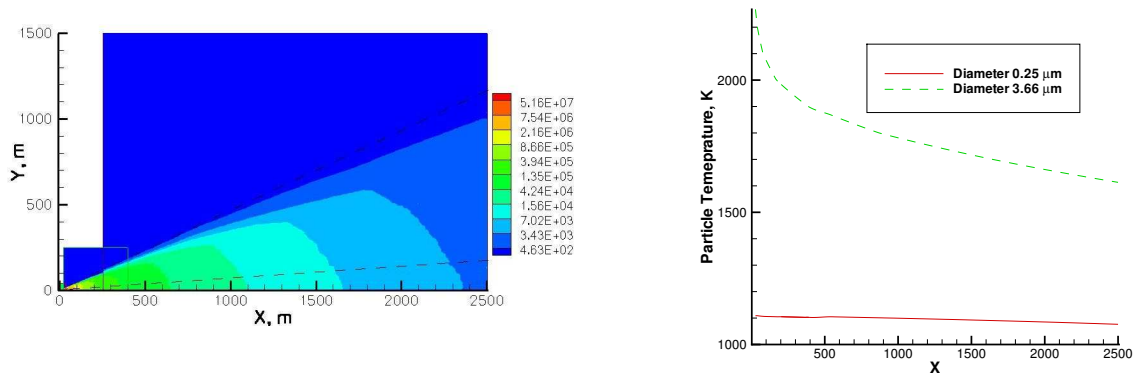

Figure 8. Left: number density per m^3 (left) for 0.25μm particles. Right: 390 nm photon scattering phase function for 0.25μm particles

The number density field of submicron particles is given in Fig. 8a. Similar to the previous figure, the dashed lines show the directions of the near field and far field photometers. It is clearly shown that there is a large number of small particles present in the field of view of the far field photometer. For any particular distance from the detector, the particle densities for 25° line of sight are within a factor of two of the corresponding values for the 4° line. It is also important that the particle number density at 25° is high enough for photon scattering to be important. Over the first several hundred meters from the nozzle, the 200 nm photon mean free path at 25° is less than 10 km, which means that a noticeable number of photons emitted in the coreflow near the nozzle axis may be scattered from submicron particles moving in the flow.

The number of photons scattered at any given angle, as a function of the scattering angle, is given in Fig. 8b. Both the actual phase function calculated with BHMIE, and the Henyey-Greenstein approximation used in the present computations, are given here for $0.25\mu m$ particles. The most important are the photons emitted in the coreflow, reflected on particles moving along the $25°$ line of sight, and scattered back to the photometer. Typical scattering angles for these photons would be in the range of $150°$-$180°$. As Fig. 8b shows, there is a significant chance of photon backscattering in this range. Note also the good agreement between BHMIE and its approximation for these angles.


Figure 9. Left: number density per m^3 (left) for 3.66μm particles. Right: particle temperatures along the nozzle axis

Photon back scattering from larger particles ($3.66\mu m$ to $11\mu m$ diameter considered in this work) to the far field photometer is expected to be negligibly small, primarily due to extremely small concentrations of these particles in the side flow. This is illustrated in Fig. 9a where the number densities of $3.66\mu m$ particles are presented. Although the maximum deflection angle for these particles is larger than $25°$, their number densities along the $25°$ line are two orders of magnitude smaller than the corresponding densities along the $4°$ line, and four orders of magnitude smaller than the submicron particle densities. Although the submicron particles are expected to be the main source of photon scattering, they are not a significant source of photon emission. This is primarily due to the relatively low temperatures of these small particles. Because of their size, they are cooled by gas molecules in the plume much faster than the larger particles. Comparison of particle temperatures for the first two particle diameter bins is given in Fig. 9. The temperature of $0.25\mu m$ particles is slightly over 1,100 K at the nozzle exit, and decreases slowly in the plume both due to radiation and gas-particle heat transfer. The temperature of the $3.66\mu m$ particles is much higher in the plume, changing from over 2,300 K at the nozzle exit to about 1,700 K two kilometers downstream.

VI.   UV Radiation from Star 27 Plume

The particle number density and temperature flow fields obtained at Steps 2, 3, and 4, were combined and interpolated to a non-uniform rectangular grid, which was used to calculate spectral radiance in the range from 200 nm to 400 nm. In order to compare numerical results with the experimental data taken by near and far field photometers,[15] the computed radiance values were integrated with a triangular filter over a 51 nm window centered at a wavelength of 230 nm. Let us first analyze the results for the $4°$ line of sight.

Comparison of the calculated UV spectral radiance with the measurements[15] is presented in Fig. 10. Note that no corrective scaling factor of any kind was used for the calculated radiance. The agreement between the calculation and experiment is very reasonable for smaller wavelengths, from 200 nm to about 300 nm. In this range, the calculated values are about 50% higher then the corresponding measurements. For the wavelengths larger than 300 nm, there is a significant difference between the two. For 400 nm, the calculation overpredicts the experimental data by over an order of magnitude. One of the most probable reasons for such a difference is inadequate values of particle emissivity used in the calculations. Generally, the expressions for the absorption index used to calculate emissivities as a function of particle size and temperature are not well known. The uncertainty in emissivity may well approach an order of magnitude.[32] Comparison of
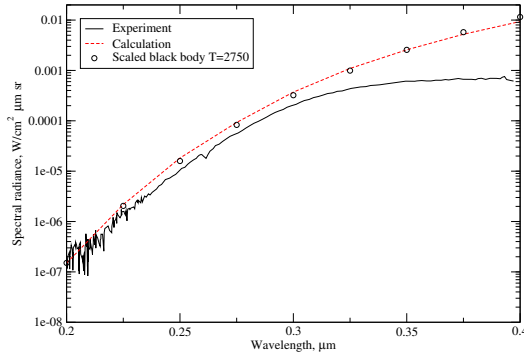
Figure 10. Comparison of computed and experimental spectra at 4°.

expressions of Ref. 28 used in this work with values calculated according to experimental recommendations of Ref. 33 shows that the experimental values for 1μm particles at 680 nm are about 6 times lower than those obtained from the expressions in Ref. 28. Obviously, 6 times lower emissivities translate to close to 6 times lower radiance at that wavelength.

Table 3. 4° line of sight computed and experimental spectral radiance (10^{-6} W/(cm^2 μm sr)) at 230 nm.

Case	Full	No scattering	Bin 1	Bin 2	Bin 3	Bin 4	Bin 5	Measurement[15]
Radiance	4.59	6.21	9.64×10^{-11}	3.16	1.85	1.07	0.39	3.6

The calculated 4° line of sight radiant intensity integrated over a 51 nm region centered at 230 nm is given in Table 3. At this wavelength, the computed value of 4.59×10^{-6} W/(cm^2 μm sr) agrees reasonably with the experimental value of 3.6×10^{-6} W/(cm^2 μm sr). Computations have also been performed with the photon scattering turned off for all particle bins ("No scattering" column) and separately for each particle bin with properties taken from the same plume flow predictions. It is clear that for the 4° line the photon scattering results decrease in radiance. This is related to the shadowing of photons emitted by larger particles by relatively cold sub-micron particles. As computations for different particle bins show, the main emitters are particles of bin 2 (3.66μm). The contribution of larger particles is smaller due to their smaller concentrations.

Table 4. 25° line of sight computed and experimental spectral radiance (10^{-9} W/(cm^2 μm sr)) at 230 nm.

Case	Full	No scattering	No bin 1	Measurement[15]
Radiance	5.71	0.021	0.021	22

Analysis of the radiant intensity at the 25° line from the plume axis shows that the photon scattering process, while decreasing radiance from the core flow, becomes the governing process for larger angles from the plume axis. For the considered 25° line, the radiation decreases from 5.71×10^{-9} W/(cm^2 μm sr) to 0.021×10^{-9} W/(cm^2 μm sr) when the scattering is turned off. The radiance computed for the last four particle bins ("No bin 1" column) coincide with that computed without scattering. This shows that all scattering occurs on sub-micron particles, and that the submicron particles' contribution to the photon emission process is negligible. The computed radiation is within a factor of four of the measured value, which is a significant improvement over the prediction of Ref. 12 where the calculated radiance was about five orders of magnitude lower than the experimental data. Note that no photon scattering was included in Ref. 12. The difference in the current prediction and the data is believed to be primarily due to a significantly larger number of submicron particles in the actual plume, compared to the size distribution assumed in this work.

VII.   Conclusions

Numerical study of a Star 27 rocket plume at an altitude of 118 km has been conducted. A combined multi-step continuum/kinetic approach has been used, with the Navier-Stokes equations being solved inside the nozzle and in the near field, and the DSMC method used in the mid and far fields. All flow solvers used in this work included two-way coupling between the gas flow and alumina particles. Comparison of the continuum and kinetic solutions in the near field showed very good agreement in the plume, both for gas and particulates, and significant differences in the plume-atmosphere interaction region.

The calculated alumina particle properties have been used to calculate spectral radiant intensities in the UV region. The results were compared with available on-board flight measurements for two lines of sight; near field ($4°$ from the plume axis) and far field ($25°$). The numerical modeling has indicated that the main process determining the far field radiation is photon scattering on submicron particles. Accounting for this effect increases the predicted radiance by a factor of 300, and the value of the full radiance at 230 nm in this case is approximately a factor of four lower than the measurements. The difference is attributed to inaccuracy in the particle size distribution assumed in the simulations. The predicted near field radiation is only about 30% higher than the measurements at 230 nm. This difference increases to approximately an order of magnitude at 400 nm due to inadequate particle emissivity used for this region.

VIII.   Acknowledgments

References

[1] Hiers, R.S., Critical Behavior in Small Particle Combustion, Journal of Thermophysics and Heat Transfer, 2000, vol.14, no.1, pp. 53-58.

[2] Rodionov, A.V., Plastinin, Yu.A., and Karabadzhak, G.F., Soot oxidation modeling in plumes, AIAA Paper 2001-3858.

[3] Miake-Lye, R.C., Martinez-Sanchez, M., Brown, R.C., et al., Stratospheric aircraft exhaust plume and wake chemistry, NASA Contractor Report 191495, 1993.

[4] Simmons, F.S. Rocket Exhaust Plume Phenomenology, The Aerospace Corporation Aerospace Press Series, Published by AIAA, 2000, 286 pages.

[5] Dr. Rainer Dressler, Private communication, 2006.

[6] Zhong, J., Zeifman, M.I., Gimelshein, S.F., and Levin, D.A. Direct Simulation Monte Carlo Modeling of Homogeneous Condensation in Supersonic Plumes, AIAA Journal, Vol.43, No.8, pp. 1784 -1796, Aug. 2005.

[7] Zhong, J., Gratiy, S., Zeifman, M.I., and Levin, D.A. Development of a Kinetic Nucleation Model for Simulation of a Free-expanding Argon Condensation in DSMC, AIAA paper 2005-4950.

[8] Ramos, A., Fernandez, J.M., Tejeda, G., Montero, S. Quantitative study of cluster growth in free-jet expansions of CO_2 by Rayleigh and Raman Scattering, Phys. Review A., 2005, Vol. 72, 053204.

[9] Kim, Y.J., Wyslouzil, B.E., Wilemski, G., Wolk, J., Strey, R. Isothermal nucleation rates in supersonic nozzles and the properties of small water clusters, J. Phys. Chemistry A, 2004, Vol. 108, No. 20, pp. 4365-4377.

[10] Reed, R.A., Calia, V.S. "Review of aluminum oxide rocket exhaust particles," AIAA Paper 93-2819.

[11] York, B., Lee, R., Sinha, N., Dash, S. "Progress in the simulation of particulate interactions in solid propellant rocket exhausts'," AIAA Paper 2001-3590.

[12] Candler, G., Levin, D., Branderburg, J., Collins, R., Erdman, P., Zipf, E., Howlett, C. Comparison of theory with plume radiance measurements from the Bow Shock Unltraviolet 2 Rocket Flight, AIAA Paper 92-0125.

[13] Gimelshein, S.F., Levin, D.A., Drakes, J.A., Karabadzhak, G.F., Plastinin, Yu.A. Modeling of Ultraviolet Radiation in Steady and Transient High-Altitude Plume Flows, Journal of Thermophysics and Heat Transfer, Vol. 16, No. 1, 2002, pp. 58-67.

[14] Gimelshein, S., Markelov, G., and Muylaert, J. Numerical Modeling of Low Thrust Solid Propellant Nozzles at High Altitudes , AIAA-2006-3273, 2006.

[15] Erdman, P.W., Zipf, E.C., Espy, P., Howlett, C., Collins, R.J., Cristou, C., Levin, D.A., Candler, G.V. In-situ measurements of UV and VUV radiation from a rocket plume and re-entry bow-shock, AIAA Paper 91-0124.

[16] Smathers, H.W., Horan, D.M., Cardon, J.D., Malaret, E.R., Singh, M., Sorensen, T., Laufer, P.M., Corson, M.R., Brandenburg, J.E., McKay, J.A., Strunce, R.R. Ultraviolet Plume Instrument Imaging from the LACE Satellite Strypi Rocket Plume, Naval Research Laboratory Report NRL/FR/8121-93-9526, Washington, DC, September 1993.

[17] Kawasaki, A. H., Coats, D. E., Berker, D. R., "A Two-Phase, Two-Dimensional, Reacting Parabolized Navier-Stokes Sover for the Prediction of Solid Rocket Moter Flowfields," AIAA Paper 92-3600.

[18] Chakravarthy, S., and Peroomian, O., "Some Internal Flow Applications of a Unified-Grid CFD Methodology," AIAA 96-2926, 32nd AIAA /ASME /SAE /ASEE Joint Propulsion Conference and Exhibit, Lake Buena Vista, FL, July 1996.

American Institute of Aeronautics and Astronautics Paper 2007-1014

[19]Peroomian, O., Chakravarthy, S., and Golberg, U., "A 'Grid Transparent' Methodology for CFD," AIAA 97-0724, 35th Aerospace Sciences Meeting and Exhibit, Reno, NV, Jan. 1997.

[20]Henderson, C.A., "Drag Coefficients of Spheres in Continuum and Rarefied Flows," AIAA Journal Vol. 14 No. 6 June 1976 pg 707-8.

[21]Ivanov , M.S., Markelov, G.N., and Gimelshein S.F. "Statistical simulation of reactive rarefied flows: numerical approach and applications," AIAA Paper 98-2669.

[22]Ivanov, M.S., Rogasinsky, S.V., "Analysis of the numerical techniques of the direct simulation Monte Carlo method in the rarefied gas dynamics," *Soviet J. Numer. Anal. Math. Modeling*, Vol. 3, No. 6, 1988, pp. 453-465.

[23]Bird, G.A., *Molecular Gas Dynamics and the Direct Simulation of Gas Flows.* Clarendon Press, Oxford. 458 pp, 1994.

[24]Walters, D.V., Buckius, R.O., Rigorous development for radiation heat transfer in nonhomogeneous absorbing, emitting and scattering media, Int.J.Heat Mass Transfer, V.35, No 12, pp.3323-3333

[25]Modest, M. F., "Backward Monte Carlo Simulations in Radiative Heat Transfer", ASME Journal of Heat Transfer, 2003, Vol. 125, No. 1, pp. 57-62.

[26]Freeman, G. N., Ludwig, C. B., Malkmus, W., and Reed, R., "Development and Validation of Standardized Infrared Radiation Model (SIRRM) Gas/Particle RadiationTransfer Model,"USAF/Air ForceRocket Propulsion Lab., AFRPL-TR-79-55,Edwards AFB, CA, Oct. 1979.

[27]Dombrovsky LA. Radiation heat transfer in disperse systems. New York: Begell House; 1996.

[28]N. A. Anfimov, G.F. Karabadjak, B. A. Khmelinin, Y.A. Plastinin and A.V. Rodionov , "Analysis of Mechanisms and Nature of Radiation from Aluminum Oxide in Different Phase States in Solid Rocket Exhaust Plumes", AIAA-93-2818, 1993

[29]Bohren, C.F., Huffman, D.R. Absorption and Scattering of Light by Small Particles (Wiley, New York, 1982), Appendix A.

[30]Ranz, W., Marshall, W., *Chem. Eng. Prog.*, **48**, 141, 1952.

[31]Rodionov, A.V., Plastinin, Y.A., Drakes, J.A., Simmons, M.A., and Hiers, R.S., Modeling of Multiphase Alumina-Loaded Jet Flow Fields, *AIAA Paper 98-3462*.

[32]Duval, R., Soufiani, A., Taine, J. Coupled radiation and turbulent multiphase flow in an alimized solid propellant rocket engine, J. Quant. Spectrocop. Radiat. Transfer, Vol. 84, 2004, pp. 513-526.

[33]Parry, D.L., Brewster, M.Q. Optical constants and size of propellant combustion aluminum oxide smoke, AIAA Paper 88-3350.